Evolving a Single Puncture Using the Moving Puncture Method*

Ann Author[†] and Second Author[‡]
Authors' institution and/or address
*This line break forced with *

(MUSO Collaboration)

Charlie Author[§]
Second institution and/or address
This line break forced and
Third institution, the second for Charlie Author

Delta Author
Authors' institution and/or address
*This line break forced with *

(CLEO Collaboration)
(Dated: October 6, 2023)

In this paper, we investigate the evolution of a single puncture within the framework of the Moving Puncture Method. The Moving Puncture Method has proven to be a powerful technique in numerical relativity for evolving black hole spacetimes. In our study, we focus on its application to the evolution of a single puncture, which can serve as a fundamental building block in simulating more complex spacetime scenarios.

Usage: Secondary publications and information retrieval purposes.

Structure: You may use the `description` environment to structure your abstract; use the optional argument of the `\item` command to give the category of each item.

I. INTRODUCTION

Since the first successful simulations of merging black-hole binaries for computing accurate gravitational waveforms, various formulations and techniques have been employed. These include the BSSN (*Baumgarte-Shapiro-Shibata-Nakamura*) formulation [1–3], conformal decompositions [4, 5], the Bowen-York approach [6], and the moving puncture gauge [7]. These methods have been in use until recently.

Evolving a Schwarzschild black hole serves as a valuable benchmark for assessing the performance of numerical codes, given that we possess its analytical solutions.

In this paper, we present a method for obtaining analytic solutions for a Schwarzschild black hole under time-independent conditions. We provide numerical setups and results for comparison with these analytical solutions.

II. INITIAL DATA

A. Spatial Metric

We need to specify the spatial metric γ_{ij} and the extrinsic curvature K_{ij} which satisfy the Hamiltonian constraint

$$R + K^2 - K_{ij}K^{ij} = 16\pi\rho, \quad (1)$$

and the momentum constraint

$$D_j(K^{ij} - \gamma^{ij}K) = 8\pi j^i. \quad (2)$$

To construct a single puncture initial data, we adopt York-Lichnerowicz conformal decompositions [4, 5]. The spatial metric is decomposed into a conformal factor ψ multiplying an conformally related metric:

$$\gamma_{ij} = \psi^4 \bar{\gamma}_{ij}. \quad (3)$$

With this, (1) turns into

$$\bar{D}^2\psi - \frac{\psi}{8}\bar{R} + \frac{\psi^5}{8}\left(K_{ij}K^{ij} - K^2\right) = -2\pi\psi^5\rho, \quad (4)$$

where we define the conformal Laplace operator

$$\bar{D}^2\psi \equiv \bar{\gamma}^{ij}\bar{D}_i\bar{D}_j\psi. \quad (5)$$

We assume

1) *vacuum spacetime* ($\rho = 0$, $j^i = 0$),

2) *time symmetry* ($\partial_t\gamma_{ij} = 0$, $\beta^i = 0$),

so the extrinsic curvature

$$K_{ij} = \frac{1}{2\alpha}\left(\mathcal{L}_\beta\gamma_{ij} - \partial_t\gamma_{ij}\right) \quad (6)$$

vanishes and also $K = 0$. Therefore, (2) satisfied identically. If we assume *conformal flatness*, the conformally related metric to be flat,

$$\bar{\gamma}_{ij} = \eta_{ij}, \quad (7)$$

---

(4) reduces to the simple Laplace equation

$$\bar{D}^2 \psi = 0, \tag{8}$$

which has the solution

$$\psi = A + \frac{B}{r}. \tag{9}$$

To satisfy asymptotically flat as $r \to \infty$, and ADM mass to be M, we should choose $A = 1$ and $B = \frac{M}{2}$:

$$\psi = 1 + \frac{M}{2r}. \tag{10}$$

TwoPunctures [8] uses the Bowen-York approach [6] and the method presented in [7]. Since there is a single puncture with neither spin nor momentum, the result should be the same as in (10). We set TP_epsilon to 10^{-6} and TP_Tiny to 0, resulting in

$$\psi = 1 + \frac{M}{2\tilde{r}}, \tag{11}$$

where

$$\tilde{r} = \left(r^4 + 10^{-24}\right)^{1/4}. \tag{12}$$

The initial metric set by TwoPunctures exactly takes the form

$$\gamma_{ij} = \left(1 + \frac{M}{2\tilde{r}}\right)^4 \eta_{ij}, \tag{13}$$

for all grid points. Fig. 1 shows γ_{xx} along the x-axis at the initial time. Each marker represents a grid point for a respective refinement level. The non-diagonal components of the spatial metric and all components of the extrinsic curvature have explicit values of 0.
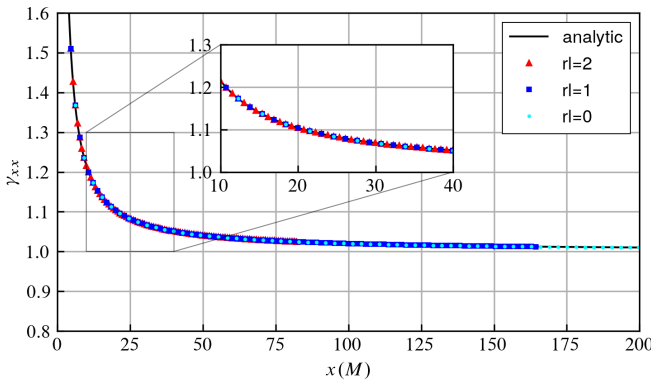
B. Constraints

From (1) and (2), we can define

$$\mathcal{H} \equiv R + K^2 - K_{ij}K^{ij} - 16\pi\rho, \tag{14}$$

$$\mathcal{M}^i \equiv D_j(K^{ij} - \gamma^{ij}K) - 8\pi j^i, \tag{15}$$

and it should satisfy that $\mathcal{H} = 0$ and $\mathcal{M}^i = 0$. Fig. 2 shows $\log_{10}|\mathcal{H}|$ on the xy plane at the initial time. Every value at each grid point is less than 10^{-7}. In the case of $\mathcal{M}^i$, all of the values are explicitly 0.
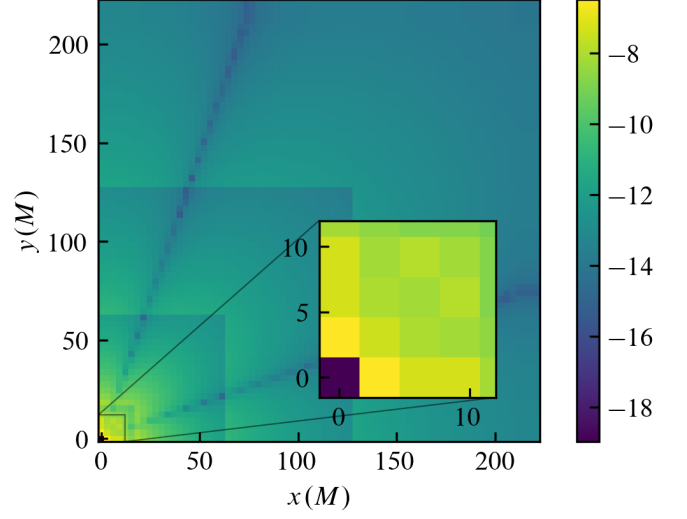

FIG. 2. $\log_{10}|\mathcal{H}|$ on the xy plane at the initial time.

Fig. 3 shows the Hamiltonian constraint violation $\mathcal{H}$ along the x axis. The data at $x = 0$ has been cut since its value is on the order of 1 at the late time. $\mathcal{H}$ increased as time passed, and most peak point's x coordinate also increased. But it still remains on the order of 10^{-6} at $t = 115.2M$.
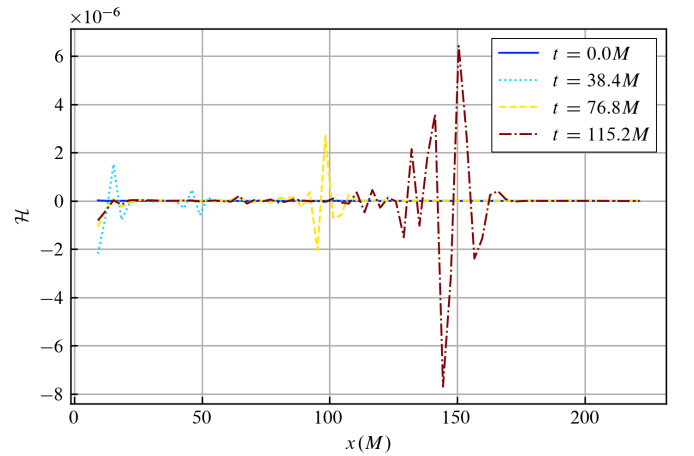

FIG. 1. γ_{xx} along the x-axis at the initial time. Only 3 of the 7 refinement levels are plotted.

FIG. 3. The Hamiltonian constraint violation along the x axis.

III. EVOLUTION

A. Gauge Condition

The 1+log slicing with advection term is given by

$$\partial_t \alpha = -2\alpha K + \beta^i \partial_i \alpha, \tag{16}$$

and the hyperbolic gamma driver condition for the shift with advection term is defined as

$$\partial_t \beta^i = \frac{3}{4} B^i + \beta^j \partial_j \beta^i, \tag{17}$$

$$\partial_t B^i = \partial_t \bar{\Gamma}^i - B^i + \beta^j \partial_j B^i, \tag{18}$$

which is typically employed in the moving puncture method [9, 10]. Sometimes we can drop the advection term, simplifying (16), (17), and (18) to

$$\partial_t \alpha = -2\alpha K, \tag{19}$$

$$\partial_t \beta^i = \frac{3}{4} B^i, \tag{20}$$

$$\partial_t B^i = \partial_t \bar{\Gamma}^i - B^i, \tag{21}$$

which we adopt in this paper.

We used the `twopunctures-averaged` initial lapse, which is given by

$$\alpha = \frac{1}{2}(1 + \alpha'), \tag{22}$$

where

$$\alpha' = \frac{1 - \frac{M}{2r}}{1 + \frac{M}{2r}}, \tag{23}$$

ensuring that the lapse satisfies $0 \le \alpha \le 1$.

When the simulation progresses sufficiently, and the solution becomes time-independent, we have $\partial_t \alpha = 0$, implying $K = 0$. Since we choose the hyperbolic gamma driver condition, it has a special solution (see [11, 12])

$$\alpha = \sqrt{1 - \frac{2M}{r_s} + \frac{27M^4}{16r_s^4}}, \tag{24}$$

where r_s is an areal radius related to the isotropic radius r as

$$r = \frac{2r_s + M + (4r_s^2 + 4Mr_s + 3M^2)^{1/2}}{4} \times \left(\frac{(4 + 3\sqrt{2})(2r_s - 3M)}{8r_s + 6M + 3(8r_s^2 + 8Mr_s + 6M^2)^{1/2}} \right)^{1/\sqrt{2}}. \tag{25}$$

The conformal factor is given by $\psi = \left(\frac{r_s}{r} \right)^{1/2}$, and when substituted into (25), we obtain

$$\psi = \left(\frac{4r_s}{2r_s + M + (4r_s^2 + 4Mr_s + 3M^2)^{1/2}} \right)^{1/2} \left(\frac{8r_s + 6M + 3(8r_s^2 + 8Mr_s + 6M^2)^{1/2}}{(4 + 3\sqrt{2})(2r_s - 3M)} \right)^{1/2\sqrt{2}}. \tag{26}$$

Fig. 4 shows α along the x axis at several times. After $t = 49.152M$, α remains almost constant. The black solid line represents the analytic solution given in (24).

Fig. 5 shows γ_{xx} along the x axis. The black solid line indicates the analytic solution $\gamma_{ij} = \psi^4 \eta_{ij}$, where ψ is given by (26).

B. BSSN

The 3+1 ADM evolution equations are given as:

$$(\partial_t - \mathcal{L}_\beta)\gamma_{ij} = -2\alpha K_{ij}, \tag{27}$$

$$(\partial_t - \mathcal{L}_\beta)K_{ij} = -D_i D_j \alpha + \alpha(R_{ij} + KK_{ij} - 2K_{ik}K^k{}_j) + 4\pi\alpha M_{ij}, \tag{28}$$

However, this set of partial differential equations is only weakly hyperbolic and is therefore not suitable for stable numerical evolution. To address this, we adopt the BSSN (*Baumgarte-Shapiro-Shibata-Nakmura*) formulation [1–3].

In the BSSN formulation, the spatial metric γ_{ij} is decomposed into a conformally related metric as in (3), with $\det(\bar{\gamma}_{ij}) = 1$. The extrinsic curvature is also decomposed into its trace and traceless parts, and we conformally transform the traceless part as follows:

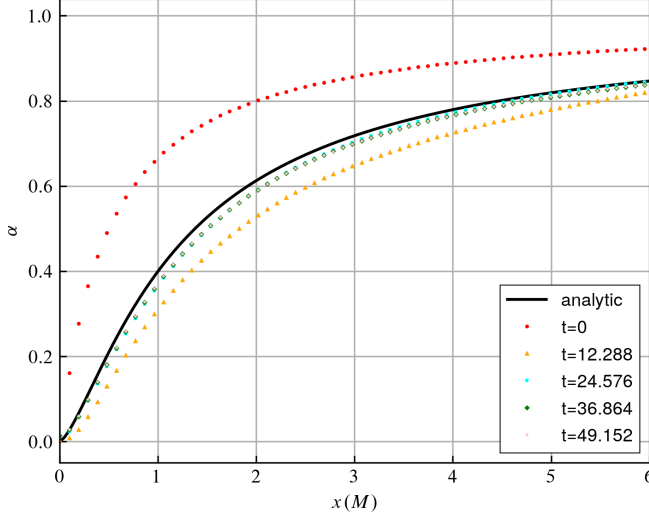$$K_{ij} = e^{4\phi} \tilde{A}_{ij} + \frac{1}{3}\gamma_{ij} K. \tag{29}$$

$$\partial_t \bar{\gamma}_{ij} = -2\alpha \tilde{A}_{ij} + \beta^k \partial_k \bar{\gamma}_{ij}$$
$$+\bar{\gamma}_{ik}\partial_j \beta^k + \bar{\gamma}_{jk}\partial_i \beta^k - \frac{2}{3}\bar{\gamma}_{ij}\partial_k \beta^k. \quad (33)$$

The evolution equation for K_{ij} also splits into two equations:

$$\partial_t K = -D^i D_i \alpha + \alpha(\tilde{A}_{ij}^{ij} + \frac{1}{3}K^2)$$
$$+\beta^i \partial_i K + 4\pi\alpha(\rho + S), \quad (34)$$

$$\partial_t \tilde{A}_{ij} = e^{-4\phi}\left[-D_i D_j \alpha + \alpha(R_{ij} - 8\pi S_{ij})\right]^{TF}$$
$$+\alpha(K\tilde{A}_{ij} - 2\tilde{A}_{ik}\tilde{A}^k{}_j) + \beta^k \partial_k \tilde{A}_{ij}$$
$$+\tilde{A}_{ik}\partial_j \beta^k + \tilde{A}_{jk}\partial_i \beta^k - \frac{2}{3}\tilde{A}_{ij}\partial_k \beta^k, \quad (35)$$

where the superscript TF denotes the trace-free part of a tensor. The Ricci tensor is also split into:

$$R_{ij} = \bar{R}_{ij} - 2\left(\bar{D}_i \bar{D}_j \phi + \bar{\gamma}_{ij}\bar{\gamma}^{lm}\bar{D}_l \bar{D}_m \phi\right)$$
$$+4\left((\bar{D}_i\phi)(\bar{D}_j\phi) - \bar{\gamma}_{ij}\bar{\gamma}^{lm}(\bar{D}_l\phi)(\bar{D}_m\phi)\right)$$
$$\equiv \bar{R}_{ij} + R_{ij}^\phi. \quad (36)$$

The $\bar{\Gamma}^i$ are now treated as independent functions that satisfy their own evolution equations:

$$\partial_t \bar{\Gamma}^i = 2\alpha\left(\bar{\Gamma}^i{}_{jk}\tilde{A}^{kj} - \frac{2}{3}\bar{\gamma}^{ij}\partial_j K - 8\pi\bar{\gamma}^{ij}S_j + 6\tilde{A}^{ij}\partial_j\phi\right)$$
$$-2\tilde{A}^{ij}\partial_j\alpha + \beta^j\partial_j\bar{\Gamma}^i - \bar{\Gamma}^j\partial_j\beta^i$$
$$+\frac{2}{3}\bar{\Gamma}^i\partial_j\beta^j + \frac{1}{3}\bar{\gamma}^{il}\partial_l\partial_j\beta^j + \bar{\gamma}^{jl}\partial_j\partial_l\beta^i. \quad (37)$$

We use the variable:

$$W = \gamma^{-1/6} = e^{-2\phi} \quad (38)$$

instead of ϕ. The evolution equation for W is:

$$\partial_t W = \frac{1}{3}W(\alpha K - \partial_i\beta^i) + \beta^i\partial_i W. \quad (39)$$

The other choice, which evolves ϕ, can lead to crashes due to numerical singularities.

We use McLachlan [13–15] and adopt the set of equations (33), (34), (35), (37), (39) for evolution and the gauge conditions (19), (20).

IV. NUMERICAL SETUP

We utilize the Einstein Toolkit [16, 17] to simulate the evolution of a single puncture.

FIG. 4. α along the x axis at several times. Only 5 refinement levels are plotted. The time unit is divided by M.
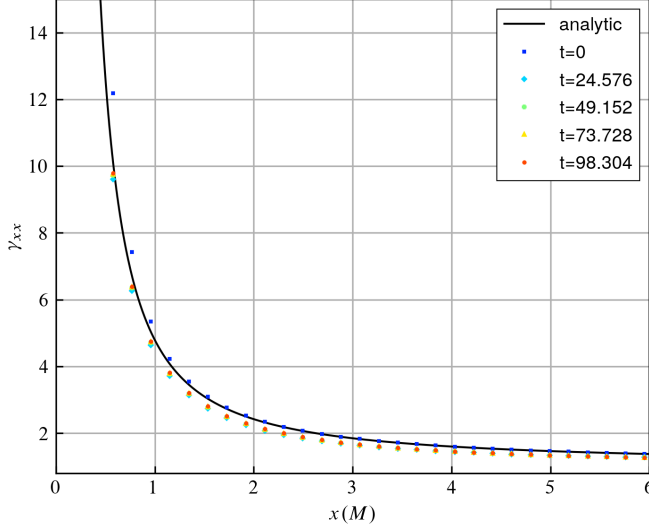
FIG. 5. γ_{xx} along the x axis at several times. Only refinement level 4 is plotted. The time unit is divided by M.

We then promote the following variables to evolution variables:

$$\phi = \ln\psi = \frac{1}{12}\ln\gamma, \quad (30)$$

as well as the conformal connection functions:

$$\bar{\Gamma}^i = \bar{\gamma}^{jk}\bar{\Gamma}^i{}_{jk} = -\partial_j\bar{\gamma}^{ij}. \quad (31)$$

The evolution equation for γ_{ij} splits into two equations:

$$\partial_t\phi = -\frac{1}{6}\alpha K + \beta^i\partial_i\phi + \frac{1}{6}\partial_i\beta^i, \quad (32)$$

A. Mesh Refinement

We employ mesh refinement [18] for the puncture center with 7 levels. The basic grid resolution is $3.072M$, and the refinement factor is set to 2. Therefore, the minimum resolution is $3.072M \times 2^{-6} = 0.048M$.

B. Boundary Conditions

We used Minkowski boundary condition in ML_BSSN. We used ghost zones size of 3.

C. Symmetry

We used REFLECTIONSYMMETRY to reflection on z plane and CARPETREGRID2 to 180° rotating symmetry.

V. RESULT

A. Gravitational Waves

For wave extraction, we utilized the WEYLSCAL4 and MULTIPOLE thorns [19]. These thorns extract the Weyl scalar and decompose it into the spin-weighted spherical harmonics. To calculate the radiated energy, we considered modes up to $l = 8$, which are considered credible because higher modes are dominated by numerical noise [20].

Since the Schwarzschild metric has spherical symmetry, there should be no gravitational wave radiation. Figure 6 displays the real and imaginary parts of $r_{\rm ex}\psi_4$. There is no notable difference between $r_{\rm ex} = 50M$. Furthermore, all values of $r_{\rm ex}\psi_4$ are on the order of 10^{-14}, which can be regarded as numerical noise.
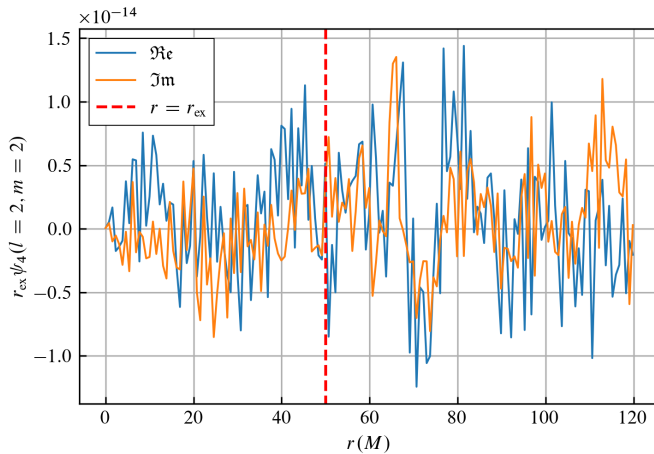

FIG. 6. Real and imaginary parts of $r_{\rm ex}\psi_4$. The red dashed line indicates $r = r_{\rm ex} = 50M$.

B. Apparent Horizon

We measured the apparent horizon at each time using AHFINDERDIRECT [21, 22]. This tool identifies an apparent horizon by numerically solving the equation

$$\Theta \equiv D_i n^i + K_{ij} n^i n^j - K = 0, \tag{40}$$

where n^i represents the outward-pointing unit normal to the apparent horizon, and D_i is the covariant derivative operator associated with the 3-metric in the slice.

We did not fix the puncture location at the origin, but there was no puncture movement, and the puncture remained at the origin. Figure 7 illustrates the expansion Θ of the apparent horizon as a function of time, while Figure 8 displays the irreducible mass $M_{\rm irr}$ as a function of time.
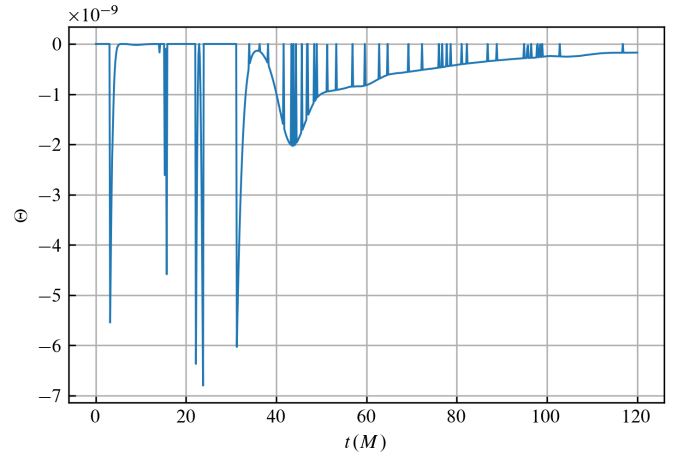

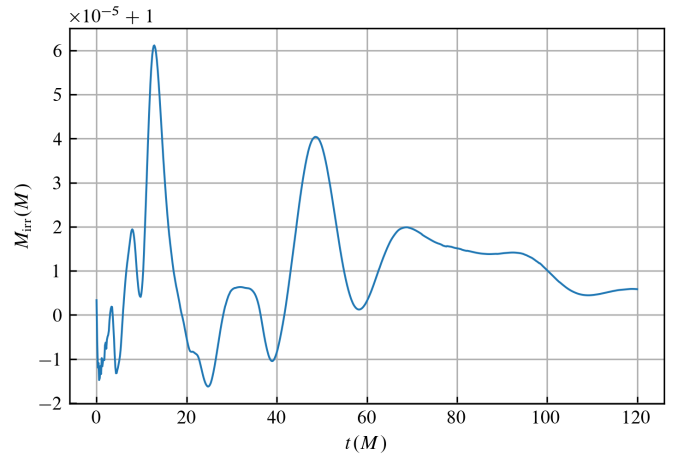FIG. 7. Expansion Θ of the apparent horizon as a function of time.

FIG. 8. Irreducible mass $M_{\rm irr}$ as a function of time.

[1] T. Nakamura, K. Oohara, and Y. Kojima, General Relativistic Collapse to Black Holes and Gravitational Waves from Black Holes, Progress of Theoretical Physics Supplement **90**, 1 (1987), https://academic.oup.com/ptps/article-pdf/doi/10.1143/PTPS.90.1/5201911/90-1.pdf.

[2] M. Shibata and T. Nakamura, Evolution of three-dimensional gravitational waves: Harmonic slicing case, Phys. Rev. D **52**, 5428 (1995).

[3] T. W. Baumgarte and S. L. Shapiro, On the numerical integration of Einstein's field equations, Phys. Rev. D **59**, 024007 (1999), arXiv:gr-qc/9810065.

[4] J. W. York, Gravitational degrees of freedom and the initial-value problem, Phys. Rev. Lett. **26**, 1656 (1971).

[5] A. Lichnerowicz, On completely harmonic Riemannian spaces, Bull. Soc. Math. Fr. **72**, 146 (1944).

[6] J. M. Bowen and J. York, James W., Time asymmetric initial data for black holes and black hole collisions, Phys. Rev. D **21**, 2047 (1980).

[7] B. Brügmann, J. A. González, M. Hannam, S. Husa, U. Sperhake, and W. Tichy, Calibration of moving puncture simulations, Phys. Rev. D **77**, 024027 (2008).

[8] M. Ansorg, B. Brügmann, and W. Tichy, A single-domain spectral method for black hole puncture data, Phys. Rev. D **70**, 064011 (2004), arXiv:gr-qc/0404056.

[9] M. Campanelli, C. O. Lousto, P. Marronetti, and Y. Zlochower, Accurate evolutions of orbiting black-hole binaries without excision, Phys. Rev. Lett. **96**, 111101 (2006), arXiv:gr-qc/0511048.

[10] M. Alcubierre, B. Brügmann, P. Diener, M. Koppitz, D. Pollney, E. Seidel, and R. Takahashi, Gauge conditions for long term numerical black hole evolutions without excision, Phys. Rev. D **67**, 084023 (2003), arXiv:gr-qc/0206072.

[11] T. W. Baumgarte and S. G. Naculich, Analytical representation of a black hole puncture solution, Phys. Rev. D **75**, 067502 (2007).

[12] M. Hannam, S. Husa, F. Ohme, B. Brügmann, and N. Ó Murchadha, Wormholes and trumpets: Schwarzschild spacetime for the moving-puncture generation, Phys. Rev. D **78**, 064020 (2008).

[13] J. D. Brown, P. Diener, O. Sarbach, E. Schnetter, and M. Tiglio, Turduckening black holes: an analytical and computational study, Phys. Rev. D **79**, 044023 (2009), arXiv:0809.3533 [gr-qc].

[14] Kranc, Kranc: Kranc assembles numerical code.

[15] McLachlan, McLachlan, a public BSSN code.

[16] L. Werneck, S. Cupp, T. Assumpção, S. R. Brandt, C.-H. Cheng, P. Diener, J. Doherty, Z. Etienne, R. Haas, T. P. Jacques, B. Karakaş, K. Topolski, B.-J. Tsao, M. Alcubierre, D. Alic, G. Allen, M. Ansorg, M. Babiuc-Hamilton, L. Baiotti, W. Benger, E. Bentivegna, S. Bernuzzi, T. Bode, G. Bozzola, B. Brendal, B. Bruegmann, M. Campanelli, F. Cipolletta, G. Corvino, R. D. Pietri, A. Dima, H. Dimmelmeier, R. Dooley, N. Dorband, M. Elley, Y. E. Khamra, J. Faber, G. Ficarra, T. Font, J. Frieben, B. Giacomazzo, T. Goodale, C. Gundlach, I. Hawke, S. Hawley, I. Hinder, E. A. Huerta, S. Husa, T. Ikeda, S. Iyer, L. Ji, D. Johnson, A. V. Joshi, H. Kalyanaraman, A. Kankani, W. Kastaun, T. Kellermann, A. Knapp, M. Koppitz, N. Kuo, P. Laguna, G. Lanferman, P. Lasky, L. Leung, F. Löffler, H. Macpherson, J. Masso, L. Menger, A. Merzky, J. M. Miller, M. Miller, P. Moesta, P. Montero, B. Mundim, P. Nelson, A. Nerozzi, S. C. Noble, C. Ott, L. J. Papenfort, R. Paruchuri, D. Pollney, D. Price, D. Radice, T. Radke, C. Reisswig, L. Rezzolla, C. B. Richards, D. Rideout, M. Ripeanu, L. Sala, J. A. Schewtschenko, E. Schnetter, B. Schutz, E. Seidel, E. Seidel, J. Shalf, K. Sible, U. Sperhake, N. Stergioulas, W.-M. Suen, B. Szilagyi, R. Takahashi, M. Thomas, J. Thornburg, C. Tian, M. Tobias, A. Tonita, S. Tootle, P. Walker, M.-B. Wan, B. Wardell, A. Wen, H. Witek, M. Zilhão, B. Zink, and Y. Zlochower, The einstein toolkit (2023), to find out more, visit http://einsteintoolkit.org.

[17] Cactus developers, Cactus Computational Toolkit.

[18] Carpet, Carpet: Adaptive Mesh Refinement for the Cactus Framework.

[19] J. G. Baker, M. Campanelli, and C. O. Lousto, The Lazarus project: A Pragmatic approach to binary black hole evolutions, Phys. Rev. D **65**, 044001 (2002), arXiv:gr-qc/0104063.

[20] D. Pollney, C. Reisswig, E. Schnetter, N. Dorband, and P. Diener, High accuracy binary black hole simulations with an extended wave zone, Phys. Rev. D **83**, 044045 (2011), arXiv:0910.3803 [gr-qc].

[21] J. Thornburg, Finding apparent horizons in numerical relativity, Phys. Rev. D **54**, 4899 (1996), arXiv:gr-qc/9508014.

[22] J. Thornburg, A Fast Apparent-Horizon Finder for 3-Dimensional Cartesian Grids in Numerical Relativity, Class. Quantum Grav. **21**, 743 (2004), arXiv:gr-qc/0306056.